CrossMark

UV-luminescent MgZnO semiconductor alloys: nanostructure and optical properties

**Dinesh Thapa[1] · Jesse Huso[1] · Kevin Miklos[1] · Peter M. Wojcik[1] · David N. McIlroy[1] ·
John L. Morrison[2] · Caleb Corolewski[3] · Matthew D. McCluskey[3] ·
Thomas J. Williams[4] · M. Grant Norton[5] · Leah Bergman[1]**

Abstract MgZnO is emerging as a vital semiconductor-alloy system with desirable optical properties that can span a large range of the UV spectrum. Due to its benign chemical character, MgZnO is considered to be an environmentally friendly material. This paper presents studies on annealing as a useful and straightforward approach for the enhancement of the optical and crystal quality of $Mg_{0.17}Zn_{0.83}O$ nanocrystalline films grown via DC sputtering. The alloys were studied via several imaging and optical techniques. It was found that high-temperature annealing, ~ 900 °C, in Argon atmosphere, significantly improves the solubility of the alloy. This temperature range is consistent with the thermal diffusion temperature of Mg needed for the creation of a soluble alloy. Moreover, the annealing process was found to minimize the undesirable visible luminescence, attributed to Mg and Zn interstitials, while significantly enhancing the bandgap sharpness and the efficiency of the UV-luminescence at ~ 3.5 eV. The analysis indicated that these optical attributes were achieved due to the combined effects of good solubility, an improved morphology, and a reduction of native defects. The annealing was also proven to be beneficial for the reduction of the compressive stress in the alloy: a relaxation ~ 1.8 GPa was calculated via Raman scattering. The inherent stress was inferred to originate mainly from the granular morphology of the alloys.

✉ Leah Bergman
lbergman@uidaho.edu

1 Department of Physics, University of Idaho, Moscow, ID 83844-0903, USA

2 Division of Natural Sciences and Mathematics, Lewis-Clark State College, Lewiston, ID 83501, USA

3 Department of Physics and Astronomy, Washington State University, Pullman, WA 99164-2814, USA

4 Electron Microscopy Center, University of Idaho, Moscow, ID 83844-0903, USA

5 School of Mechanical and Materials Engineering, Washington State University, Pullman, WA 99164-2814, USA

1 Introduction

$Mg_xZn_{1-x}O$, where x is the composition, is emerging as an important alloy system with optical properties that can span a large range of the UV spectrum ~ 3.3–7.7 eV (~ 375–161 nm) [1–7]. This semiconductor can be utilized in conjunction with, or as an alternative to, $Al_xGa_{1-x}N$, both of which are needed in UV technology [8]. ZnO and MgO are wide-bandgap semiconductors: ZnO has a bandgap ~ 3.3 eV, while that of MgO is ~ 7.7 eV [9, 10]. Zn and Mg have comparable atomic size; thus, alloying is achievable which results in a change of the bandgap of one end-member to the other, depending on the alloy composition. The crystal structure of ZnO is hexagonal wurtzite, while that of MgO is cubic rocksalt. The different crystal structure of the two end-members impedes the realization of a complete solid-solution, of the $Mg_xZn_{1-x}O$ alloy system [11, 12]. Achieving good solubility depends generally on the growth techniques and on post-growth treatments such as annealing.

In addition to the engineered bandgaps of the $Mg_xZn_{1-x}O$ system, another advantage is the alloys' capability to luminesce. One crucial aspect for the utilization of $Mg_xZn_{1-x}O$ as absorbers or light emitters is the optimization of their bandgap properties and the enhancement of the UV luminescence. This paper presents studies on the material and optical properties of wurtzite $Mg_{0.17}Zn_{0.83}O$

alloy nanocrystalline films that were grown by a reactive DC magnetron sputtering technique. As-grown and Argon annealed samples were studied via scanning electron microscopy (SEM), X-ray diffraction (XRD), atomic force microscopy (AFM), transmission, photoluminescence (PL), and micro-Raman scattering. The as-grown alloy was found to be segregated into Zn-rich and Mg-rich domains, had poor morphology, and exhibited defect-related PL in the visible range while the UV-PL was weak. Annealing at 900 °C under Argon atmosphere was found to significantly improve the nanostructure, solubility, and optical properties of the alloy, specifically that of the desired UV luminescence. Moreover, the inherent internal compressive stress in the nanocrystalline film was found to relax upon annealing.

2 Experiments

$Mg_{0.17}Zn_{0.83}O$ alloy films were grown by reactive DC magnetron sputtering using custom Zn–Mg targets (99.99 %) with 30 W of power and (0001) sapphire substrates. In this paper we will refer to the alloys as MgZnO. The chamber was evacuated to a base pressure of 10^{-6} Torr before growth. A total working chamber pressure of 11 mTorr was used, with high purity Ar as the working gas and high purity O_2 as the reactive gas. The gas flow was held constant throughout the experiment using MKS p4b mass flow controllers. The substrates were held at a constant temperature of 250 °C throughout growth. The thickness of the films were ∼350 nm. Two as-grown samples were annealed for 1 h under flowing, high purity Ar gas: one at 750 °C and another at 900 °C. The annealing experiments were performed utilizing a Lindberg/Blue M quartz tube furnace controlled by a Yokogawa UP-150 temperature controller. The as-grown sample was placed in a cleaned alumina boat and was inserted into the quartz tube. The inlet and the outlet gas flexible-tubes were connected via compression fittings. Initially the gas lines were purged at room-temperature for 10 min, setting the Ar flow-rate at 1255 cm³/min. Subsequently, the Ar flow rate was reduced to 273 cm³/min and the annealing process was started.

The photoluminescence experiments were carried out using a JY-Horiba Fluorolog-3 spectrometer with an excitation source of a Xe lamp. The cold temperature, 77 K, Raman and PL measurements were performed utilizing a Jobin–Yvon T64000 micro Raman and PL system in conjunction with an Instec 621 V microcell customized for UV measurements. The transmission spectra were collected at room temperature using an Agilent Cary 300 spectrophotometer operating in double beam mode to remove substrate effects. The film composition was determined to be ∼17 % Mg by energy dispersive X-ray

spectroscopy (EDS). The surface morphology of the films was examined utilizing SEM. The structural properties of the films were determined by XRD using a Siemens Diffractometer D5000 with the Cu Kα1 line operating in 2–theta mode.

3 Results and discussion

3.1 SEM and XRD: morphology related studies

The surface morphology of the as-grown and the two Ar annealed films were studied via SEM, and representative images are presented in Fig. 1b–d For comparison
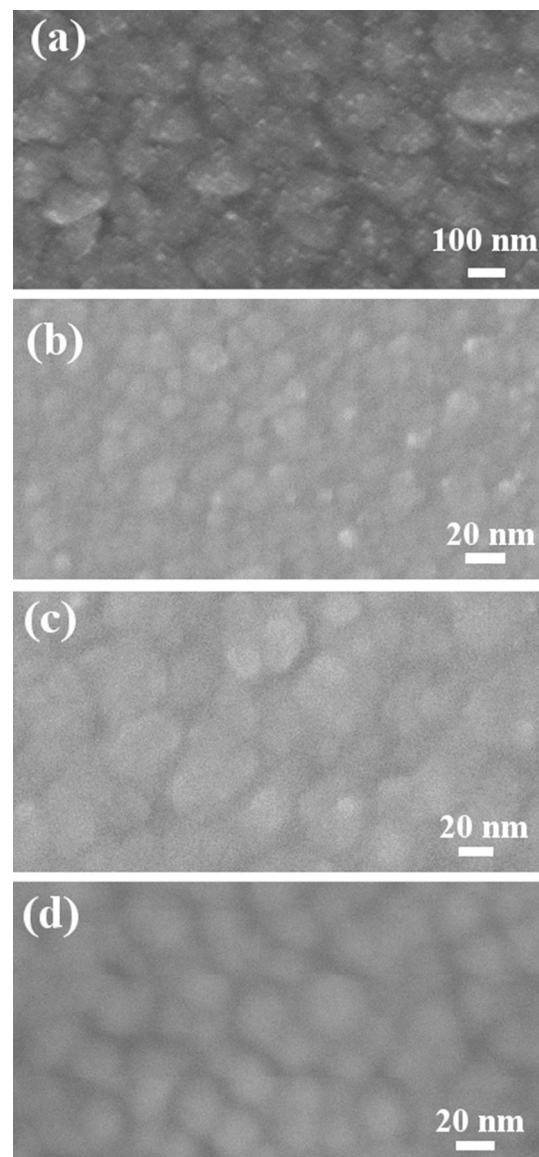

Fig. 1 The SEM images of: **a** ZnO as-grown film, **b** MgZnO as-grown, **c** MgZnO 750 °C annealed, and **d** MgZnO 900 °C annealed. The magnification of the SEM is 180 kX

purposes an image of an as-grown ZnO film is also included (Fig. 1a. As can be seen in Fig. 1b, the as-grown MgZnO film displays a rough granular morphology with small grains of size ∼10 nm, which is much smaller that of the as-grown ZnO ∼100 nm. The reduced grain size in MgZnO alloy films has been previously observed [13, 14]. The XRD of the alloy films is presented in Fig. 2, indicating the preferential c-axis orientation of the wurtzite structure and a successive improvement of material quality upon annealing.

As will be discussed in a later section, the PL spectrum of the as-grown MgZnO film exhibits two peaks in the UV region, as can be seen in Fig. 6. One peak is at 3.25 eV, attributed to Zn-rich domains, and the other is at 3.50 eV, attributed to Mg-rich domains, implying that the MgZnO is not fully alloyed. Due to the incomplete alloyed nature of the as-grown film, it is reasonable to assume that some of the MgO is in aggregate form in the grain boundaries. It has been previously reported that MgO in alumina ceramics acts as a grain size suppressor via the solute drag mechanism [15]. This mechanism involves the segregation of solute material to a grain boundary, which impedes grain boundary motion resulting in small grains. Similar behavior of grain growth impediment due to MgO has been also observed and analyzed for ZnO and ZnO-V2O5 varistors doped with Mg [16, 17]. In these studies, an inverse correlation was found between the mole percent of the MgO to the grain size: the higher the percent the smaller the grain size [16, 17]. The effect of MgO on the film's
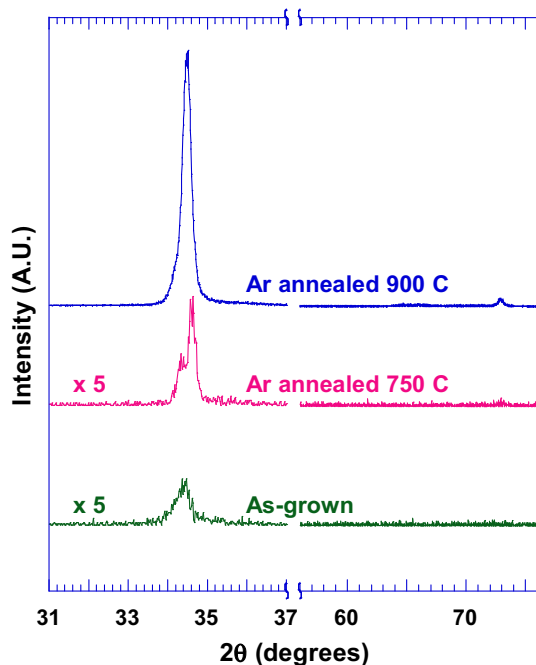
microstructure may explain the difference in the grain size between the as-grown MgZnO and the ZnO films observed in our study.

Upon annealing at 750 °C, the smaller grains in that sample appear to agglomerate forming coarse clusters of grains as can be seen in Fig. 1c. During annealing at this temperature, intermixing between the Zn-rich and Mg-rich wurtzite phase is initiated, and the MgO aggregates in the grain boundary may incorporate into the grains. The onset of the alloying process is further evidenced from the observed single broad UV-PL peak (Fig. 6) and the relatively improved XRD. In a previous study by our group on $Mg_{0.10}Zn_{0.90}O$ ceramic, an onset of alloying was found to take place ∼800–900 °C which concurs with the present results [18]. Additionally, in MgZnO thin film grown via pulse laser deposition (PLD), it was reported that a temperature ∼850 °C was required for the thermal diffusion of Mg to create the alloy [19].

In contrast to the morphology of the as-grown, the image of the 900 °C annealed film presented in Fig. 1d shows an improved morphology with larger well-defined and smooth grains. To gain further knowledge on the surface morphology of the 900 °C annealed alloy, AFM analysis was conducted, and its result is presented in Fig. 3. As can be seen in the AFM images, the granular surface has a smoothness of only a few nano-meters: the height profile analysis indicated that the average surface roughness is ∼8.5 nm (with RMS value ∼1.6 nm). This surface quality may be understood in terms of the lateral growth of the grains in the annealed film. After annealing at 900 °C, the MgZnO film is expected to be fully alloyed, an assertion which is also supported by the significantly enhanced UV-PL peak 3.45 eV (Fig. 6) and by the significantly improved XRD peak as can be seen in Fig. 2. The rather smooth and lateral surface morphology can be understood in terms of the suppression of c-axis due to the addition of the MgO with rock salt structure. Similar results to ours have been reported previously for MgZnO film grown via the Magnetron co-sputtering [20]. Also, in sol–gel MgZnO films, the addition of Mg was reported to markedly improve the surface flatness of the films [13].

3.2 Bandgap properties: transmission and urbach analysis

Transmission spectroscopy may yield valuable information regarding the electronic structure of a semiconductor including its bandgap energy and the extent of the in-gap defect states. The bandgap energy can be ascertained via Tauc analysis, while the in-gap properties can be studied via Urbach analysis [21, 22]. These two methods are well-established and commonly used for the investigation of semiconductor properties [23–25]. Figure 4 presents the
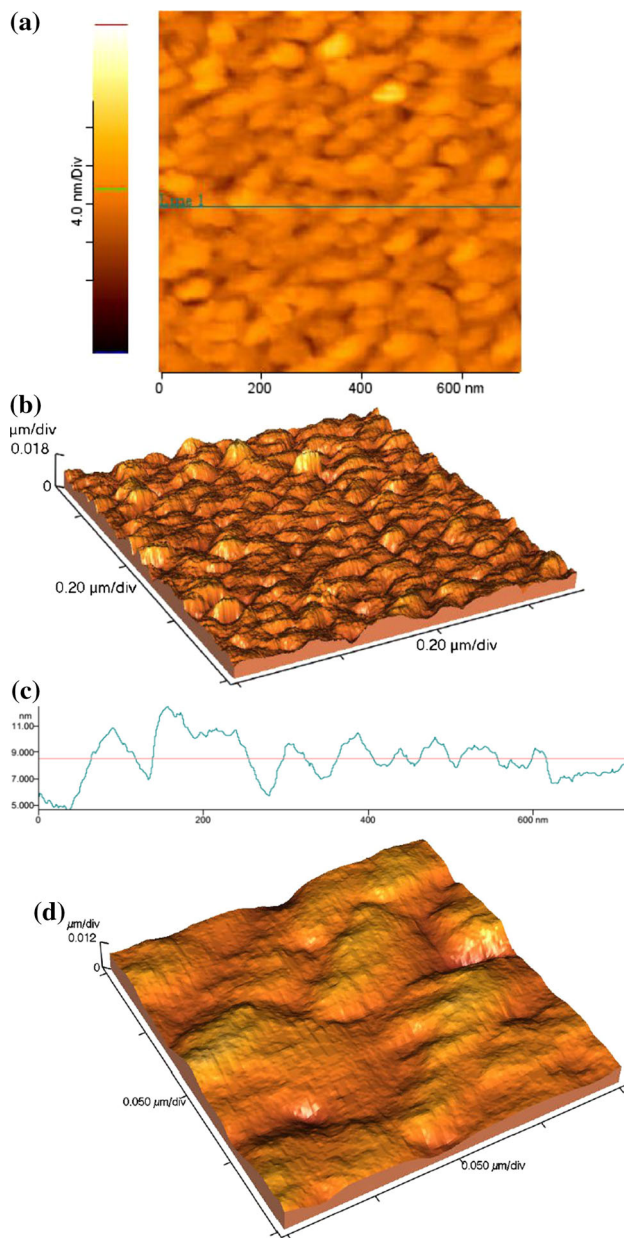

Fig. 2 The XRD of the MgZnO films: the as-grown, and that of both annealed samples

Fig. 3 The AFM images of the 900 °C annealed MgZnO: **a** a top view image, and **b** a side view: both images show an area ~700 nm × 700 nm. **c** The height profile extracted from the *line* in the *upper figure*; the *scale* of the axis is in nm. **d** A zoomed-in area ~200 nm × 200 nm

Fig. 4 The transmission spectra of the three MgZnO films. The *inset* is the Urbach energy analysis. Urbach energy is 97 meV for the as-grown film, 52 meV for the 750 °C annealed film, and 45 meV for the 900 °C annealed film

transmission spectra of the as-grown and the two annealed samples; the inset is the Urbach analysis. Figure 5 depicts the Tauc analysis for the MgZnO samples and that for an annealed ZnO sample. As indicated in Fig. 5, the bandgap of the three alloys are very similar ~3.5 eV, while that of ZnO is at 3.29 eV; a bandgap shift of ~200 meV was achieved via alloying.

Typically, the presence of defects in a semiconductor alloy that include impurities, structural disorders, and alloy compositio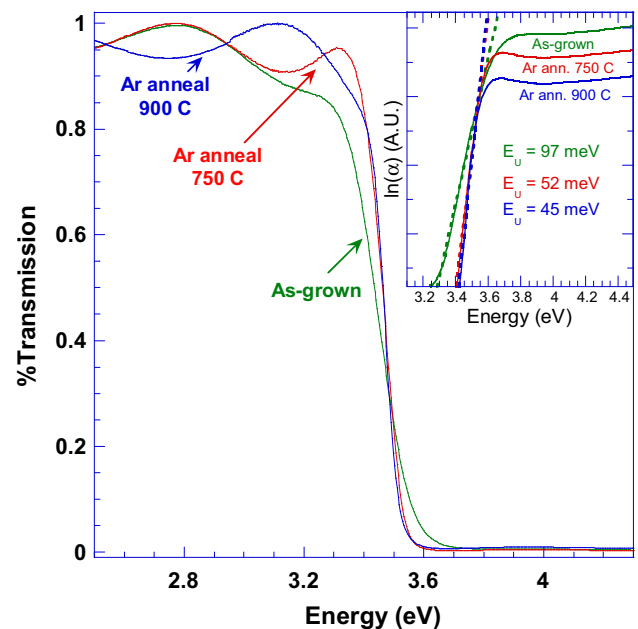nal fluctuations as well as phase segregation, are known to produce the localized energy states (band tail) within the bandgap, and a good measure of the extent of these states may be given by the Urbach energy, E_U [7, 26]. According to the Urbach model, the absorption coefficient below the optical bandgap follows exponential dependence with the photon energy, i.e., $\alpha(E) = Ce^{E/E_U}$ where $\alpha(E)$ is the absorption coefficient as a function of energy, and C is a constant. The inset to Fig. 4 presents the Urbach energy analysis for the alloys, which yields E_U values of 97 meV for the as-grown film, 52 meV for the 750 °C annealed film, and 45 meV for the 900 °C annealed film.

The gradual reduction in the Urbach energy of the films as a function of annealing temperature implies the trend of defect elimination. One type of defect is the morphology of the film. As is evident from the SEM and the XRD analyses discussed above, the film morphology was step-wise improved, starting as a degraded morphology for the as-grown film and improving as a function of annealing temperature. Another type of defect of impact that will be discussed in detail in the following section is the domain segregation in the alloy, which was significantly reduced upon increasing annealing temperature.

3.3 Photoluminescence: from the visible to the UV range of the spectrum

As can be seen in Fig. 6, the visible PL of the as-grown sample exhibits a broad PL centered at ~2.3 eV. Such visible PL has been observed and studied by several groups
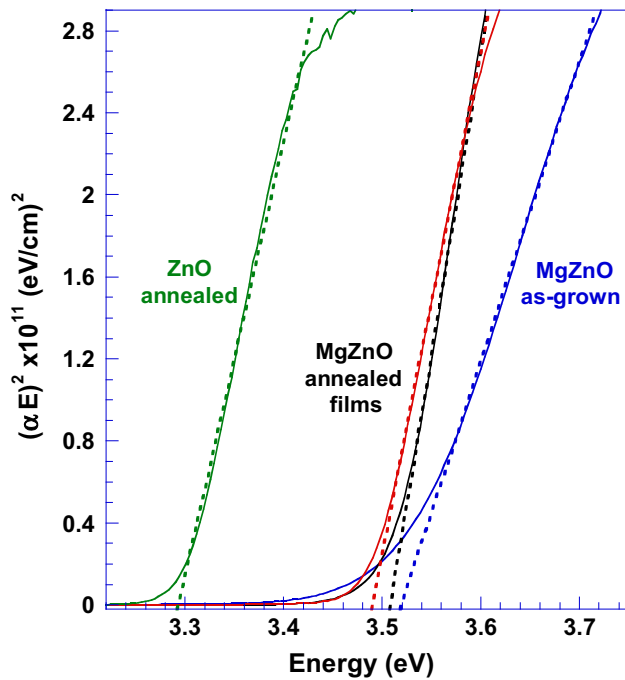
Fig. 5 The Tauc plots for the determination of the bandgaps. The as-grown alloy has a bandgap of 3.52 eV, that of the 750 °C annealed is 3.51 eV, and for the 900 °C annealed film is 3.49 eV. The bandgap of the ZnO Argon annealed is 3.29 eV. A shift of ∼0.2 eV was achieved via alloying

Fig. 6 The PL spectra of the three alloys acquired at room-temperature. The as-grown exhibit visible PL at ∼2.30 eV and two UV-emissions, one at 3.25 eV attributed to segregation of Zn–rich domains, and the other at 3.50 eV due to Mg-rich domains. The UV-PL of the 750 °C annealed film is a broad linewidth ∼192 meV attributed to a residual segregation. The UV-PL properties of the 900 °C is significantly improved: it has enhanced intensity ∼4 times that of the 750 °C annealed film, and a narrower linewidth ∼163 meV

in ZnO material [27, 28]. The general consensus is that a visible PL in the range of 2.3–2.4 eV, referred to as the green PL, is mainly due to oxygen vacancy (V_O) native defects in ZnO [27–29]. Since our alloy has relatively low Mg composition, one may expect that its green PL is in a similar energy range as that of ZnO. Further insight into the origin of the green PL of the MgZnO can be inferred from the annealing studies. Figure 6 indicates that upon annealing at 750 and 900 °C the green PL at ∼2.3 eV was significantly diminished, and a weak PL at ∼2.18 eV appeared. This is in contrast with previous studies that have shown that annealing in reduction atmospheres, such as N_2:H_2, and argon gases, has the tendency to increase the green PL [27, 29]. Additionally, studies via XRD and resistivity of annealed ZnO have indicated the loss of oxygen due to evaporation, which in turn resulted in the creation of V_O [30].

Another important factor to consider in order to understand the origin of the green PL with relation to V_O in the MgZnO, is the issue of the formation energy of vacancies during growth. Density functional calculations found that the vacancy formation energy of oxygen in ZnO is 7.01 eV, while in MgO it is much higher at 10.08 eV [31]. This implies that in MgZnO, due to the presence of Mg ions, the creation of V_O should be less thermodynamically favorable than in ZnO. There are emerging reports that
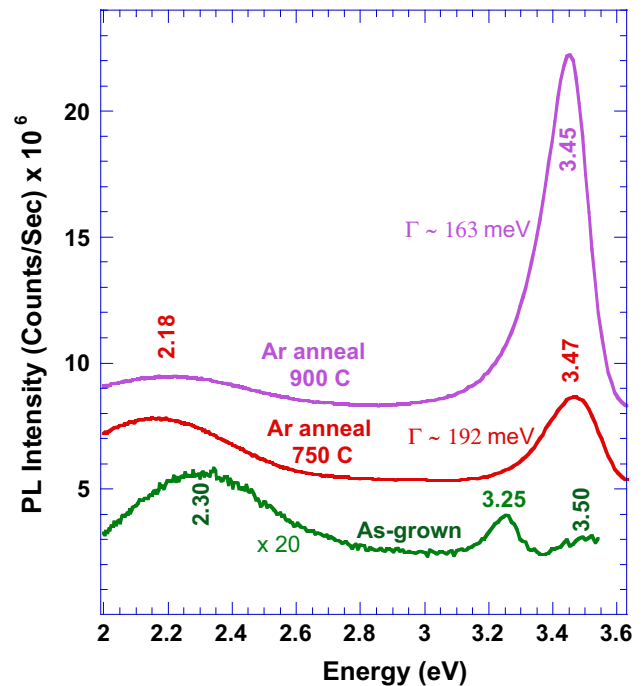
MgZnO might be a viable component in ZnO-based transistor technology due to its lower V_O defects that may improve device performance [32, 33]. In light of the above discussion we suggest that the 2.3 eV emission in our MgZnO is not due to V_O. Previous work by Trunk *et al.* on $Mg_xZn_{1-x}O$ films grown by metal–organic vapor phase epitaxy have suggested that the PL at ∼2.30 eV is due to transitions that involve intrinsic shallow donors to deep acceptors [34]. Such transitions can occur between Zn_i and O_i energy levels, and possibly Mg_i to O_i [34]. As is discussed below, our annealing experiments support this assertion.

As can be seen in Fig. 6, the 2.3 eV PL-band was almost entirely diminished after the annealing procedure, indicating the removal of some of its related native defects. It is expected that during annealing under Ar atmosphere, most interstitial defects diffuse out or incorporate into the lattice sites. While the migration barrier for Zn_i in $Mg_xZn_{1-x}O$ is not currently available, the low migration barrier for Zn_i in ZnO [35–37] suggests that any Zn_i related defects will diffuse out rapidly upon annealing of the alloy. From density–functional calculations, Janotti et al. reported the migration barrier of Zn_i to be 0.57 eV, which is considered

to be relatively low [35]. Alternatively, the mobility temperature of these defects, which was previously found to be ∼170 K [38], is significantly lower than our annealing temperature range at 1173 and 1023 K (for further discussion on the stability of Zn_i in our samples see [39]). In light of these properties, it is reasonable to expect that Zn_i related defects should be eliminated by out- diffusion as well as via incorporation into substitution lattice sites, thus diminishing the 2.3 eV PL emission. Our previous work on MgZnO ceramics found that the onset of Mg diffusion is ∼800–900 °C [18]; a similar diffusion temperature was found for MgZnO films grown via pulsed laser deposition [19]. These findings may imply that Mg atoms, via annealing as in the case of Zn_i, may be removed from their interstitial sites into lattice substitutions or out-diffused, thus diminishing the radiative recombination of the 2.3 eV. With regard to the relative weak PL at 2.18 eV that appears upon annealing (see Fig. 6), tentatively we associate it with the small concentration of vacancy or interstitial-type defects that were created during the anneal process.

One of the key desirable features among the optical properties of MgZnO alloys is their bandedge UV luminescence capability. In has been previously demonstrated that the UV-PL of ZnO can be profoundly enhanced via annealing [39]. Less work has been done regarding this topic for MgZnO alloys, specifically for sputtered alloys [40–42].

An annealing study on m-plane MgZnO, grown via metal organic chemical vapor deposition (MOCVD), was presented previously [40]. In that study nitrogen and oxygen were used as the annealing environment at an annealing temperature of 800 °C. The main conclusions regarding the enhancement of the UV luminescence was that annealing in nitrogen was proven to be very beneficial for the improvement of the UV intensity, while the oxygen environment was found to decrease that intensity. The increase in the UV-PL intensity was attributed to incorporation of Mg and to the localization of the excitons [40]. Due to the different growth methods, the MOCVD films have a planar-like morphology, in contrast to the granular morphology of our samples grown via the sputtering technique. As film morphology can be very detrimental to the light efficiency, a better comparison could be carried out with studies on MgZnO films grown using a similar technique to ours [41, 42]. In-situ annealing studies of sputtered MgZnO films under an oxygen environment and vacuum was previously conducted [41]. That study indicated that annealing in a high vacuum environment was the superior route for the improvement of the ratio of the intensity of the UV/deep level emission. Moreover, the annealing process resulted in an increase of the grain sizes and in improved morphology [41]. Additionally, annealing investigations of MgZnO sputtered films at a temperature range of 450–750 °C in air have indicated the significant improvement of the granular morphology at ∼750 °C [42]. This research was not on the UV-PL enhancement, but rather focused, among other topics, on the interesting issues of resistivity and index of refraction of MgZnO films. It was shown that at an annealing temperature of 750 °C , the resistivity of the film was considerably lowered, and that at 650 °C the index of refraction had its maximum value [42].

The novelty of our research lies in the fact that a comprehensive investigation was conducted that strictly focused on the mechanisms impacting the enhancement of the UV photoluminescence in sputtered MgZnO films with an intermediate composition range of Mg. In addition, for the annealing procedure a controllable argon atmosphere was used which is a nonvolatile environment. One of the tangible outcomes of this research concerns the relatively low growth temperature of our samples at 250 °C . Due to practical reasons it is advantageous to deposit the alloys in relatively low temperatures. This is a cost-effective mode of growth; the heater in the growth chamber is expensive, and moreover the low temperatures may prevent the corrosion of the chamber by the oxygen in the plasma. In that regard, post growth annealing in a conventional furnace, described in the "Experiments" section, becomes very beneficial for the improvement of the optical and structural properties of the alloys.

Figure 6 demonstrates the impact of annealing on the UV emission of our MgZnO films. As can be seen in Fig. 6, the effect of annealing at the two elevated temperatures is the diminishing of the doublet peaks one at 3.25 eV, attributed to Zn–rich domains in the MgZnO alloy, and the other at 3.5 eV attributed to Mg-rich domains. The annealing temperatures of 750–900 °C are well within the range of Mg and Zn thermal diffusions [18, 19], which facilitates an improved mixing of the alloy constituents. The PL line width of the 750 °C annealed sample ∼192 meV is considered to be quite broad, reflecting the existence of residual segregation. The narrowing of the line to ∼163 meV for the 900 °C annealed film indicates the improved solubility of this sample.

The other optical impact of annealing, as was discussed above, is the reduction of native defects that luminesce at ∼2.3 eV. This defect reduction eliminates a competing route to the UV luminescence in the MgZnO bandgap which contributes to the efficiency of the bandedge UV luminescence. Specifically, for the 900 °C annealed film, the significant enhancement of the UV-PL relative to that of the as grown film is a combined effect of being a more complete soluble alloy, an improved morphology, and a reduction of native defects. It bears noting that annealing of MgZnO at much higher temperatures may not be a stable route for optimizing the optical properties of the
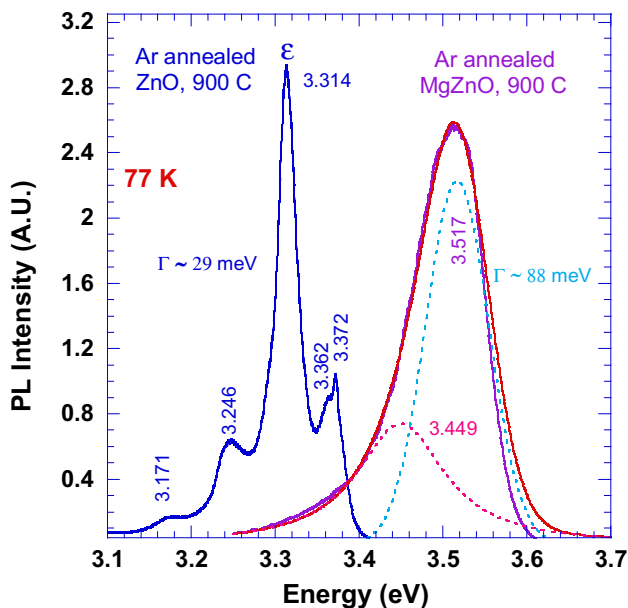
Fig. 7 The 77 K UV-PL spectrum of the MgZnO 900 °C annealed film. For comparison, the PL of a ZnO film is included that indicates its emission characteristics: excitons at the high energy range, ε-emission at 3.314 eV, and phonon replicas at the lower energy range. The PL of the alloy exhibits broadening, attributed to the random distribution of the atomic Mg and Zn substitution atoms which masks the fine structure of the luminescence. The fit to the data shows the main PL at 3.517 eV, and its phonon-replica

Fig. 8 The 77 K Raman spectra of the LO mode of the as-grown alloy and that of the 900 °C annealed sample. The ~ 9 cm^{-1} Raman shift between the two spectra is attributed to stress relaxation initiated by the high-temperature annealing

alloy. The high vapor pressure of Zn may cause its out-diffusion, changing the composition of a given alloy to become a more Mg-rich [1].

The impact of a random distribution of the atomic constituents in ternary semiconductor alloys is to broaden the PL linewidth significantly relative to that of the pure end-members. This is a well-known phenomenon, referred to as the alloy or inhomogeneous broadening, which takes place even in high-quality epitaxial films such as Al$_x$Ga$_{1-x}$As, and is due to fluctuation in the distribution of the substitution atoms, Zn and Mg in our case [43]. Figure 7 presents the PL at 77 K of annealed MgZnO and that of annealed ZnO films. Both samples have similar granular morphology. The UV-PL of the ZnO shows the expected emissions of the excitons and the ε-emission which is characteristic to nanocrystalline-type ZnO studied previously in our papers [4, 39]. The key issue is that in contrast to the ZnO, the PL of the MgZnO is featureless and broad with a linewidth ~ 88 meV, This implies that even at the relatively low Mg composition ~ 17 % the impact of the inherent alloy random distribution is quite significant.

3.4 Raman scattering and internal stress in the film

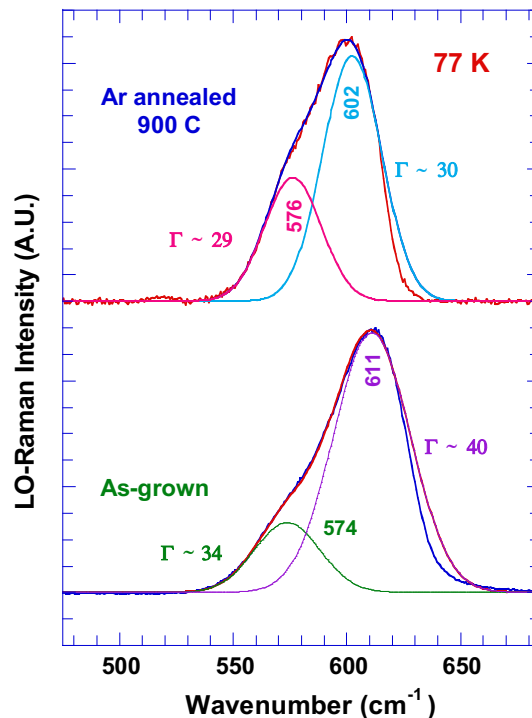In addition to improved solubility and optical properties, annealing is also expected to relax the internal stress in the films. In general, Raman scattering has proven to be a highly sensitive spectroscopy, enabling the assessment of a material's internal stress via the frequency shift of a particular Raman mode. In our experiments, Raman spectra were acquired in a back scattering geometry at 77 K utilizing the 325 nm (3.81 eV) HeCd laser line. The experimental error is $\sim \pm 1$ cm^{-1}. Since that excitation energy is close to the bandgap of the MgZnO, resonant Raman scattering occurs, resulting in enhanced LO-mode [44]. Figure 8 presents the Raman spectra of the two samples of interest: the as-grown as a reference, and that of the 900 °C annealed films. As can be seen in Fig. 8, the LO-mode exhibits a shift towards the lower frequency: it is at 611 cm^{-1} for the as-grown sample, and 602 cm^{-1} for the annealed one; i.e., a total shift of ~ 9 cm^{-1}. The shift towards the lower frequency may be suggestive of a relaxation of intrinsic compressive stress.

The pressure coefficient $\left(\frac{\partial \omega}{\partial P}\right)$ for the LO-mode in Mg$_{0.2}$Zn$_{0.8}$O (where ω is the phonon frequency) was obtained previously by our group to be ~ 4.9 cm^{-1}/GPa [45]. Since the observed Raman shift is ~ 9 cm^{-1}, a relaxation of ~ 1.8 GPa took place upon annealing. Furthermore, this relaxed stress of ~ 1.8 GPa is comparable to those obtained previously via XRD and curvature measurement studies of ZnO thin films grown via the sputtering method [46, 47]. Additionally, in our previous study of

ZnO nanocrystalline films grown via the sputtering technique, Raman analysis has indicated a similar relaxation upon annealing of ~ 1 GPa [39]. Thus, the compressive stress in our as-grown MgZnO sample can be attributed mainly to morphology, and to some extent to defect aggregations, both of which were significantly reduced during the annealing process.

The deconvolution of the Raman peak indicates that in addition to the principle Raman line, a broad peak at lower energy phonon scattering is present, as can be seen in Fig. 8. Our previous study of LO-phonon dynamics in $Mg_{0.2}Zn_{0.8}O$ nanoalloys has concluded that the principle mechanism that activates such low frequency mode is scattering due to a disorder state of the nanoalloys as is expected in random type alloy distribution [48].

3.5 Significance of alloys, and a novel ZnO-based alloy system

Alloys and semiconductor compounds are an extremely versatile type of material due to their applications in a wide range of technologies. For example, transition-metal chalcogenides have uses in photovoltaics devices, rechargeable battery electrodes, and electrochromic displays [49–51]. Metal selenides specifically also have applications as biological fluorescent labels, and extensive efforts have been made to understand their characteristics [52–54]. The nitride-based alloys such as InGaN and AlGaN are very important semiconductors for optoelectronic applications spanning the visible to the deep UV range of the spectrum [55, 56].

In this work, an oxide-based alloy, MgZnO, was investigated in order to address its UV luminescence. Achieving the UV range is also feasible with another oxide-based alloy, BeZnO, for which the substituting agent is the Be atom [57]. However, the scope of our effort is to explore alloys that are relatively environmentally friendly, which excludes the use of Be due to its high toxicity. Moreover, due to the large size of the Be atom, the BeZnO alloy system has significant phase segregation issues [57].

An emerging ZnO-based alloy is ZnS_xO_{1-x} for which the substituting agent in ZnO is the sulfur atom [58–60]. This new alloy system can reach the visible range, which makes ZnO an extremely useful semiconductor host material with tunable optical bandgap from the visible to the UV depending on the substituting atoms and their concentrations. ZnS_xO_{1-x} is a highly-lattice mismatched system, and thus is challenging to realize. Our preliminary experiments presented in Fig. 9 shows that an optical gap at the visible range ~ 2.6 eV was realized for $ZnS_{0.16}O_{0.84}$ [59, 60]. Future work will address the optical and material properties of the ZnS_xO_{1-x} alloys.
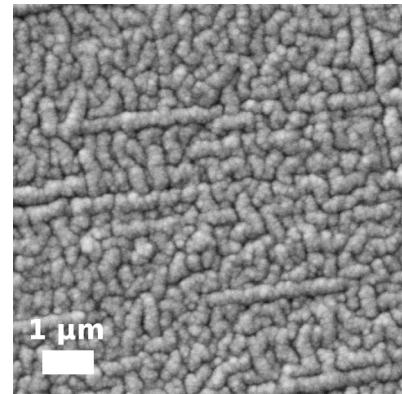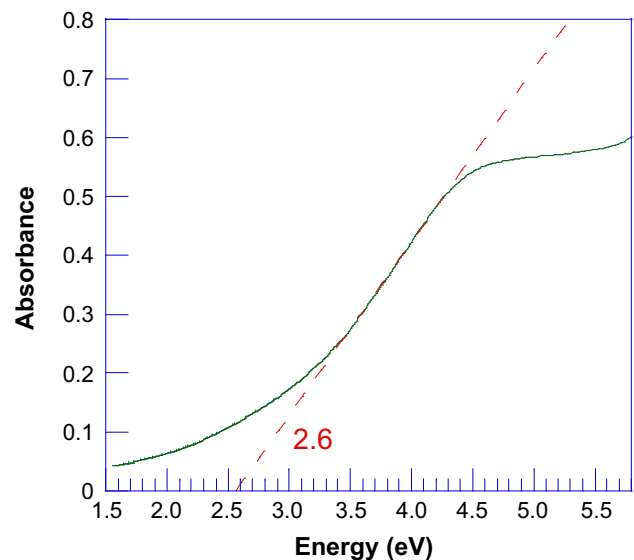

Fig. 9 The absorbance spectra and SEM image of the $ZnS_{0.16}O_{0.84}$ nanocrystalline film

4 Conclusions

$Mg_{0.17}Zn_{0.83}O$ alloy films with the wurtzite structure were grown by reactive DC magnetron sputtering. The as-grown alloy was found to be non-totally soluble: it exhibits UV-PL emissions characteristic of Zn-rich and Mg-rich segregated domains. Additionally, this sample has degraded morphology, and was found to have pronounced visible PL due to native defects associated with Zn and Mg interstitials. Annealing at 750 and 900 °C under Argon atmosphere improved the overall structural and optical properties of the alloys. Specifically, the 900 °C annealing temperature was found to be an ideal temperature-range for the achievement of a soluble alloy with a sharp bandgap, weak visible PL, and enhanced and well-defined UV-PL. The linewidth of UV-PL of that alloy was found to be broader relative to that of ZnO, which is attributed to the random nature of the alloy distribution. Moreover, annealing was proven advantageous for the relaxation of the residual internal stress in the alloy.

References

1. A. Ohtomo, M. Kawasaki, T. Koida, K. Masubuchi, H. Koinuma, Y. Sakurai, Y. Yoshida, Y. Yasuda, Y. Segawa, Appl. Phys. Lett. **72**, 2466–2468 (1998)
2. S.K. Pandey, S. Pandey, V. Awasthi, A. Kumar, M. Gupta, V. Sathe, S. Mukherjee, J. Mater. Sci. Mater. Electron. **25**, 772–777 (2014)
3. X. Wang, K. Saito, T. Tanaka, M. Nishio, T. Nagaoka, M. Aita, Q. Guo, Appl. Phys. Lett. **107**, 022111 (2015)
4. J.L. Morrison, J. Huso, H. Hoeck, E. Casey, J. Mitchell, L. Bergman, M.G. Norton, J. Appl. Phys. **104**, 123519 (2008)
5. L. Bergman, J.L. Morrison, X.-B. Chen, J. Huso, H. Hoeck, Appl. Phys. Lett. **88**, 023103 (2006)
6. J. Huso, J.L. Morrison, J. Mitchell, E. Casey, H. Hoeck, C. Walker, L. Bergman, W.M. Hlaing Oo, M.D. McCluskey, Appl. Phys. Lett. **94**, 061919 (2009)
7. J. Huso, H. Che, D. Thapa, A. Canul, M.D. McCluskey, L. Bergman, J. Appl. Phys. **117**, 125702 (2015)
8. W. Shan, J.W. Ager III, K.M. Yu, W. Walukiewicz, E.E. Haller, M.C. Martin, W.R. McKinney, W. Yang, J. Appl. Phys. **85**, 8505–8507 (1999)
9. Ü. Özgür, Y.I. Alivov, C. Liu, A. Teke, M.A. Reshchikov, S. Doğan, V. Avrutin, S.-J. Cho, H. Morkoç, J. Appl. Phys. **98**, 041301 (2005)
10. D.M. Roessler, W.C. Walker, Phys. Rev. Lett. **17**, 319–320 (1966)
11. J. Chen, W.Z. Shen, N.B. Chen, D.J. Qiu, H.Z. Wu, J. Phys.: Condens. Matter **15**, L475–L482 (2003)
12. D. Thapa, J. Huso, H. Che, M. Huso, J.L. Morrison, D. Gutierrez, M. Grant Norton, L. Bergman, Appl. Phys. Lett. **102**, 191902 (2013)
13. C.-Y. Tsay, M.-C. Wang, S.-C. Chiang, Mater. Trans. **49**, 1186–1191 (2008)
14. T. Murakawa, T. Fukudome, T. Hayashi, H. Isshiki, T. Kimura, Phys. Status Solidi C **1**, 2564–2568 (2004)
15. I.-W. Chen, Mater. Sci. Eng. A **166**, 51–58 (1993)
16. A. Smith, G. Gasgnier, P. Abélard, J. Am. Ceram. Soc. **73**(4), 1098–1099 (1990)
17. H.H. Hng, K.Y. Tse, Ceram. Int. **34**, 1153–1157 (2008)
18. J.L. Morrison, J. Huso, H. Che, D. Thapa, M. Huso, M.G. Norton, L. Bergman, J. Mater. Sci. Mater. Electron. **23**, 437–444 (2012)
19. A. Ohtomo, R. Shiroki, I. Ohkubo, H. Koinuma, M. Kawasaki, Appl. Phys. Lett. **75**, 4088–4090 (1999)
20. S.W. Kang, Y.Y. Kim, C.H. Ahn, S.K. Mohanta, H.K. Cho, J. Mater. Sci. Mater. Electron. **19**, 755–759 (2008)
21. J. Tauc, R. Grigorovici, A. Vancu, Phys. Status Solidi B **15**, 627–637 (1966)
22. J.I. Pankove, *Optical Processes in Semiconductors* (Dover, New York, 1975)
23. T. Aschenbrenner, H. Dartsch, C. Kruse, M. Anastasescu, M. Stoica, M. Gartner, A. Pretorius, A. Rosenauer, T. Wagner, D. Hommel, J. Appl. Phys. **108**, 063533 (2010)
24. A.M. El-Naggar, J. Appl. Phys. **109**, 023508 (2011)
25. S. Dutta, S. Chattopadhyay, D. Jana, A. Banerjee, S. Manik, S.K. Pradhan, M. Sutradhar, A. Sarkar, J. Appl. Phys. **100**, 114328 (2006)
26. C.W. Teng, J.F. Muth, Ü. Özgür, M.J. Bergmann, H.O. Everitt, A.K. Sharma, C. Jin, J. Narayan, Appl. Phys. Lett. **76**, 979–981 (2000)
27. K. Vanheusden, C.H. Seager, W.L. Warren, D.R. Tallant, J.A. Voigt, Appl. Phys. Lett. **68**, 403–405 (1996)
28. F.H. Leiter, H.R. Alves, A. Hofstaetter, D.M. Hofmann, B.K. Meyer, Phys. Status Solidi B **226**, R4–R5 (2001)
29. S. Ning, P. Zhan, Q. Xie, W. Wang, Z. Zhang, J. Mater. Sci. Technol. **31**, 969–978 (2015)
30. S. Dutta, M. Chakrabarti, S. Chattopadhyay, D. Jana, D. Sanyal, A. Sarkar, J. Appl. Phys. **98**, 053513 (2005)
31. J. Carrasco, N. Lopez, F. Illas, Phys. Rev. Lett. **93**, 225502 (2004)
32. C.-J. Ku, Z. Duan, P.I. Reyes, Y. Lu, Y. Xu, C.-L. Hsueh, E. Garfunkel, Appl. Phys. Lett. **98**, 123511 (2011)
33. S.-T. Lien, J.-Z. Chen, Y.-J. Yang, C.-C. Hsu, I.-C. Cheng, Ceram. Int. **40**, 2707–2715 (2014)
34. M. Trunk, V. Venkatachalapathy, A. Galeckas, A.Y. Kuznetsov, Appl. Phys. Lett. **97**, 211901 (2010)
35. A. Janotti, C.G. Van de Walle, Rep. Prog. Phys. **72**, 126501 (2009)
36. A. Janotti, C.G. Van de Walle, J. Cryst. Growth **287**, 58–65 (2006)
37. D.G. Thomas, J. Phys. Chem. Solids **3**, 229–237 (1957)
38. M.D. McCluskey, S.J. Jokela, J. Appl. Phys. **106**, 071101 (2009)
39. D. Thapa, J. Huso, J.L. Morrison, C.D. Corolewski, M.D. McCluskey, L. Bergman, Opt. Mater. **58**, 382–389 (2016)
40. A.L. Yang, H.P. Song, D.C. Liang, H.Y. Wei, X.L. Liu, P. Jin, X.B. Qin, S.Y. Yang, Q.S. Zhu, Z.G. Wang, Appl. Phys. Lett. **96**, 151904 (2010)
41. Y.Y. Kim, C.H. An, H.K. Cho, J.H. Kim, H.S. Lee, E.S. Jung, H.S. Kim, Thin Solid Films **516**, 5602–5606 (2008)
42. J. Li, J.-H. Huang, W.-J. Song, Y.-L. Zhang, R.-Q. Tan, Y. Yang, J. Cryst. Growth **314**, 136–140 (2011)
43. E.F. Schubert, E.O. Göbel, Y. Horikoshi, K. Ploog, H.J. Queisser, Phys. Rev. B **30**, 813–820 (1984)
44. L. Bergman, X.-B. Chen, J. Huso, J.L. Morrison, H. Hoeck, J. Appl. Phys. **98**, 093507 (2005)
45. J. Huso, J.L. Morrison, L. Bergman, M.D. McCluskey, Phys. Rev. B **87**, 125205 (2013)
46. V. Gupta, A. Mansingh, J. Appl. Phys. **80**, 1063–1073 (1996)
47. W.L. Dang, Y.Q. Fu, J.K. Luo, A.J. Flewitt, W.I. Milne, Superlattices Microstruct. **42**, 89–93 (2007)
48. J. Huso, J.L. Morrison, H. Hoeck, E. Casey, L. Bergman, T.D. Pounds, M.G. Norton, Appl. Phys. Lett. **91**, 111906 (2007)
49. A. Sobhani, M. Salavati-Niasari, J. Alloys Compd. **617**, 93–101 (2014)
50. A. Sobhani, M. Salavati-Niasari, J. Alloys Compd. **625**, 26–33 (2015)
51. A. Sobhani, M. Salavati-Niasari, J. Mol. Liq. **219**, 1089–1094 (2016)
52. A. Sobhani, M. Salavati-Niasari, J. Mol. Liq. **220**, 334–338 (2016)
53. A. Sobhani, M. Salavati-Niasari, J. Mater. Sci. Mater. Electron. **26**, 6831–6836 (2015)
54. A. Sobhani, M. Salavati-Niasari, J. Mater. Sci. Mater. Electron. **27**, 293–303 (2016)
55. A.M. Fischer, Y.O. Wei, F.A. Ponce, M. Moseley, B. Gunning, W.A. Doolittle, Appl. Phys. Lett. **103**, 131101 (2013)
56. S. Corekci, M.K. Ozturk, B. Akaoglu, M. Cakmak, S. Ozcelik, E. Ozbay, J. Appl. Phys. **101**, 123502 (2007)
57. M. Chen, D. Yong, C. Wu, Z. Shen, A. Chen, Y. Zhu, B. Pan, Z. Tang, J. Alloys Compd. **658**, 636–641 (2016)

58. M. Jaquez, K.M. Yu, M. Ting, M. Hettick, J.F. Sanchez-Royo, M. Welna, A. Javey, O.D. Dubon, W. Walukiewicz, J. Appl. Phys. **118**, 215702 (2015)

59. J. Huso, H. Che, J.L. Morrison, D. Thapa, M. Huso, S. Rhodes, B. Blanchard, W.J. Yeh, M.D. McCluskey, L. Bergman, in *MRS Proceedings*, vol. 1394. doi:10.1557/opl.2012.417 (2012)

60. H. Che, J. Huso, J.L. Morrison, D. Thapa, M. Huso, W.J. Yeh, M.C. Tarun, M.D. McCluskey, L. Bergman, J. Nanomater ID article 963485 (2012)